ADVANCED MATERIALS INTERFACES
www.advmatinterfaces.de

Bioinspired Tough and Strong Fibers with Hierarchical Core–Shell Structure

Yao Xiao, Chenjing Yang, Xiaowei Zhai, Lai Zhao, Peng Zhao, Jian Ruan, Dong Chen, David A. Weitz, and Kai Liu**

Strong and tough bio-based fibers are attractive for both fundamental research and practical applications. In this work, strong and tough hierarchical core–shell fibers with cellulose nanofibrils (CNFs) in the core and regenerated silk fibroins (RSFs) in the shell are designed and prepared, mimicking natural spider silks. CNF/RSF core–shell fibers with precisely controlled morphology are continuously wet-spun using a co-axial microfluidic device. Highly-dense non-covalent interactions are introduced between negatively-charged CNFs in the core and positively-charged RSFs in the shell, diminishing the core/shell interface and forming an integral hierarchical fiber. Meanwhile, shearing by microfluidic channels and post-stretching induce a better ordering of CNFs in the core and RSFs in the shell, while ordered CNFs and RSFs are more densely packed, thus facilitating the formation of non-covalent interactions within the fiber matrix. Therefore, CNF/RSF core–shell fibers demonstrate excellent mechanical performances; especially after post-stretching, their tensile strength, tensile strain, Young's modulus, and toughness are up to 635 MPa, 22.4%, 24.0 GPa, and 110 MJ m^{-3}, respectively. In addition, their mechanical properties are barely compromised even at −40 and 60 °C. Static load and dynamic impact tests suggest that CNF/RSF core–shell fibers are strong and tough, making them suitable for advanced structural materials.

1. Introduction

Strong and tough fibers, which are essential for applications in artificial tendons, surgical sutures, and body armors,[1] have attracted intensive attention.[2] High tensile strength and high toughness often conflict with each other and could not be achieved simultaneously in synthetic polymers.[3] However, in natural fibers, spider dragline silks from Nephila edulis, for example, possess both high tensile strength (1.1 GPa), high toughness (160 MJ m^{-3}), and large Young's modulus (10 GPa), making them attractive for structural materials.[4] In natural spider silks, the secondary structures of the spidroin proteins are the key to their superior mechanical performances: a series of proteins strung together into interconnected β-sheet crystallite and amorphous domains. In addition, natural spider silks generally have a core–shell microstructure, which also plays an important role for their superior mechanical performances;[5] the core, which consists of highly-aligned densely-packed elastic nanofibrils, is surrounded

Y. Xiao, P. Zhao, J. Ruan, D. Chen
Department of Medical Oncology
The First Affiliated Hospital
School of Medicine
Zhejiang University
Hangzhou, Zhejiang Province 310003, P. R. China
E-mail: chen_dong@zju.edu.cn

Y. Xiao, C. Yang, X. Zhai, D. Chen
College of Energy Engineering and State Key Laboratory of Clean Energy Utilization
Zhejiang University
Hangzhou, Zhejiang Province 310003, P. R. China

Y. Xiao, D. Chen
Zhejiang Key Laboratory of Smart Biomaterials
College of Chemical and Biological Engineering
Zhejiang University
Hangzhou, Zhejiang Province 310027, P. R. China

The ORCID identification number(s) for the author(s) of this article can be found under https://doi.org/10.1002/admi.202201962.

L. Zhao
Department of Urology
China-Japan Union Hospital of Jilin University
Changchun 130033, China

D. A. Weitz
John A. Paulson School of Engineering and Applied Sciences
Harvard University
Cambridge, MA 02138, USA

K. Liu
State Key Laboratory of Rare Earth Resource Utilization
Changchun Institute of Applied Chemistry
Chinese Academy of Sciences
Changchun 130022, China

K. Liu
Department of Chemistry
Tsinghua University
Beijing 100084, China
E-mail: kailiu@tsinghua.edu.cn

DOI: 10.1002/admi.202201962

by a thin plastic shell, which provides the protection and enhances the tensile strength.[6] However, the widespread applications of natural spider silks are limited by their low supply.[7]

Bioinspired design of regenerated fibers provides a promising strategy to achieve strong and tough biobased fibers in large quantities. The rapid developments of synthetic biology have made the large supply of raw biomaterials accessible.[8] However, the mechanical properties of regenerated biobased fibers with a single composition or a simple structure are barely satisfactory, and a lot of efforts have been dedicated to improve their mechanical performances via the fiber composition and the spinning process. For example, stiff components, such as cellulose nanocrystals,[9] cellulose nanofibrils (CNFs),[10] graphene oxides,[11] and carbon tubes,[12] are doped into the fibers to reinforce the tensile strength, and microchannels are designed to spin the fibers to achieve a better ordering in the microstructure and thus a better performance in mechanical properties.

Despite the advances, it is still difficult to control the hierarchical microstructure of regenerated biobased fibers and the ordering of nanofibrils within the fibers. Therefore, the mechanical performances of regenerated biobased fibers are often far below those of natural spider silks.[13] In addition, surface and interface engineering is also vital for mechanical performances and it is still challenging to diminish the interface between doping components and fiber matrix to form an integral fiber. Therefore, it is still an unmet need to simultaneously achieve high tensile strength and high toughness in regenerated biobased fibers.

Herein, strong and tough hierarchical cellulose nanofibril/regenerated silk fibroin (CNF/RSF) coreshell fibers mimicking natural spider silks are designed and prepared continuously in situ by a coaxial microfluidic device.[14] Regenerated silk fibroins (RSFs) originated from silkworm silks,[15] which are rich in β sheets, α helixes, and random coils,[16] are chosen as the tough shell material. CNFs extracted from building blocks of wood, which possess a super high aspect ratio of $L/D > 150$ and a super large Youngs modulus of $E > 130$ GPa,[17] are chosen as the stiff core material. CNF/RSF coreshell fibers nicely combine the advantages of tough RSFs and strong CNFs. By adjusting the inner and outer phase flow rates, the morphology and mechanical property of CNF/RSF fibers are precisely controlled. Compared with RSF fibers, CNF/RSF coreshell fibers poststretched by six times demonstrate a remarkable tensile strength of 635 MPa, a large tensile strain of 22.4%, a high Youngs modulus of 24.0 GPa and an excellent toughness of 110 MJ m^{-3}. The highlyordered and denselypacked microstructure within poststretched fibers is investigated by smallangle Xray scattering (SAXS) in detail, which facilitates the formation of nonbovalent interactions and thus enhances mechanical performances.

2. Results and Discussions

2.1. Design and Preparation of Hierarchical CNF/RSF Fibers

Spider silks are well known for their tough and strong mechanical properties and their coreshell microstructure, which consists of a stiff strong shell and a tough elastic core, plays an important role in their excellent mechanical performances.[5,18] To mimic spider silks and achieve tough and strong fibers, CNF/RSF coreshell fibers are prepared via wet spinning as shown in Figure 1a. Stiff CNFs dispersed in water, which are prepared from birch wood pulp (Figures S1 and S3a, Supporting Information), are used as the inner core, and tough RSFs dissolved in formic acid, which are prepared from silkworm cocoons (Figures S2 and S3b, Supporting Information), are used as the outer shell. When CNF and RSF solutions are extruded from the inner and outer channels of a coaxial microfluidic device (Figure S4a, Supporting Information), respectively, both the inner and outer phases are sheared by the tapered nozzles, which mimic the sharply shrunk structure at the end of the spider glandular duct,[19] and form a coaxial flow at the outlet.[20] Due to the low Reynolds number, the coaxial flow of the inner CNF and outer RSF phases forms a continuous hierarchical CNF/RSF coreshell fiber after coagulation, which is then collected and dried on a rotator. During the coagulation process, RSFs in the outer shell undergo a conformation transition, forming a network of αhelix and βsheet, which is confirmed by Fourier transform infrared spectroscopy (FTIR), as shown in Figure S5, Supporting Information. When RSFs are treated with ethanol, the infrared spectra show that the positions of the three peaks of amide I, II, and III band become stronger and sharper. The deconvolution results of amide I show that the content of βsheet and βturn increase, while αhelix decreased after RSFs treated with ethanol.[21] Meanwhile, shearaligned CNFs are protonated by formic acid from the outer shell, forming highlydense hydrogen bonds between neighboring CNFs,[22] as shown in Figure 1b. CNFs with a negative Zeta potential of -33.4 ± 2.4 mV are rich in carboxyl and hydroxyl groups and RSFs with a positive Zeta potential of 29.9 ± 3.8 mV are rich in amino groups, as shown in Figure S6, Supporting Information. FTIR spectra of the frequency range of 3550–3200 cm^{-1} representing the –OH stretching from the interand intramolecular hydrogen bonds shift and become sharper and stronger in the CNF/RSF composite, which demonstrates the strong interaction of the CNFs and RSFs through the hydrogen bonds,[23] as shown in Figure S7, Supporting Information. Therefore, nonbovalent interactions, such as hydrogen bonding and electrostatic interaction (Figure S8, Supporting Information), are expected to form between the inner core and outer shell, thus diminishing the core/shell interface and forming an integral hierarchical fiber. Moreover, a small amount of glycerin is added to the coagulation bath as plasticizer to make the CNF/RSF coreshell fibers stronger and tougher.[24] Postbstretching of asbspun CNF/RSF fibers is performed to enhance the mechanical performances using two rotators rotating at two different angular velocities, as shown in Figure 1c.

2.2. Tunable Morphology and Mechanical Property of Hierarchical CNF/RSF Fibers

CNFs are filamentlike (Figure S9, Supporting Information) and CNFs in the inner phase are strongly sheared in the converging microfluidic channel near the tapered outlet. Therefore, CNFs in the core are orientationally aligned along the fiber axis under the shearing force. When the fiber axis makes an angle

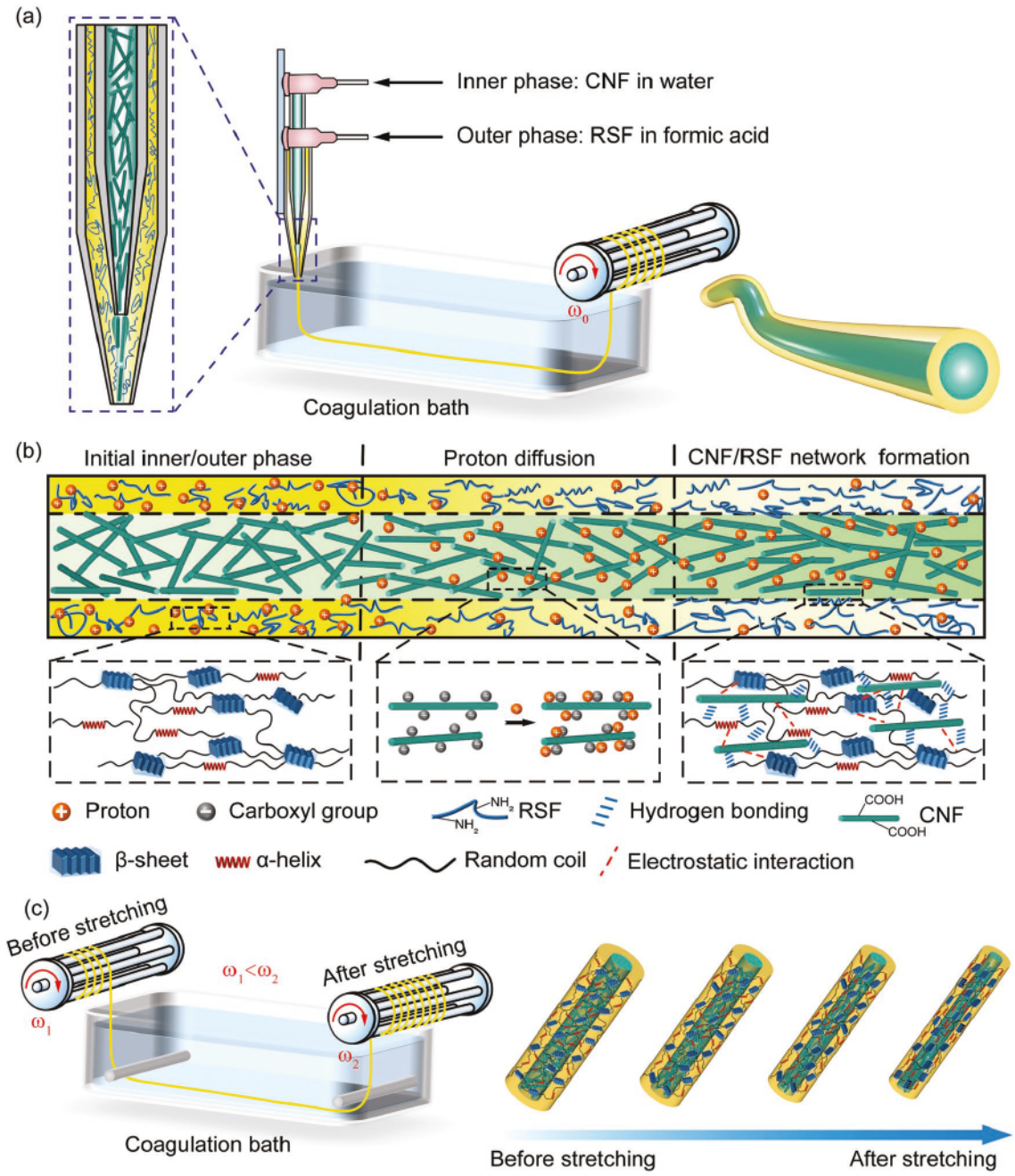

Figure 1. Design and fabrication of CNF/RSF core-shell fibers. a) Preparation of core-shell fibers with a CNF core and an RSF shell using a coaxial microfluidic device via wet spinning. The coagulation bath consists of 60 vol% ethanol, 20 vol% glycerin, and 20 vol% water. b) Schematics illustrating the non-covalent interactions within the core-shell fibers, including hydrogen bonding, van der Waals force, and electrostatic interaction. c) Post-stretching of CNF/RSF fibers via two rotators rotating at two different angular velocities. After post-stretching, CNFs and RSFs are orientationally aligned along the fiber direction, facilitating the non-covalent interactions and enhancing the mechanical performances.

with the polarizers, the core of core-shell fibers shows a high birefringence, suggesting an orientationally ordered arrangement of CNFs in the core, as shown in Figure 2a. In addition to core-shell fibers, spindle-knot fibers, which are prepared under different flow rates of the inner and outer phases, also suggest that CNFs in the core are sheared aligned.

To systematically investigate the influence of flow rates of the inner CNF and outer RSF phases on the fiber morphology, the phase diagram demonstrating different hierarchical CNF/RSF fibers prepared under different flow rates is shown in Figure 2b. When the flow rate of the outer RSF phase is greater than that of the inner CNF phase by more than 10 L min^{-1}, spindle-knot fibers form, suggesting that thicker RSF shell is more susceptible to Rayleigh instability.[25] When the flow rate of the outer RSF phase is comparable or smaller than that of the inner CNF phase, core-shell fibers are obtained. However, when the flow rate of the outer RSF phase is much smaller than that of the inner CNF phase, for example, by more than

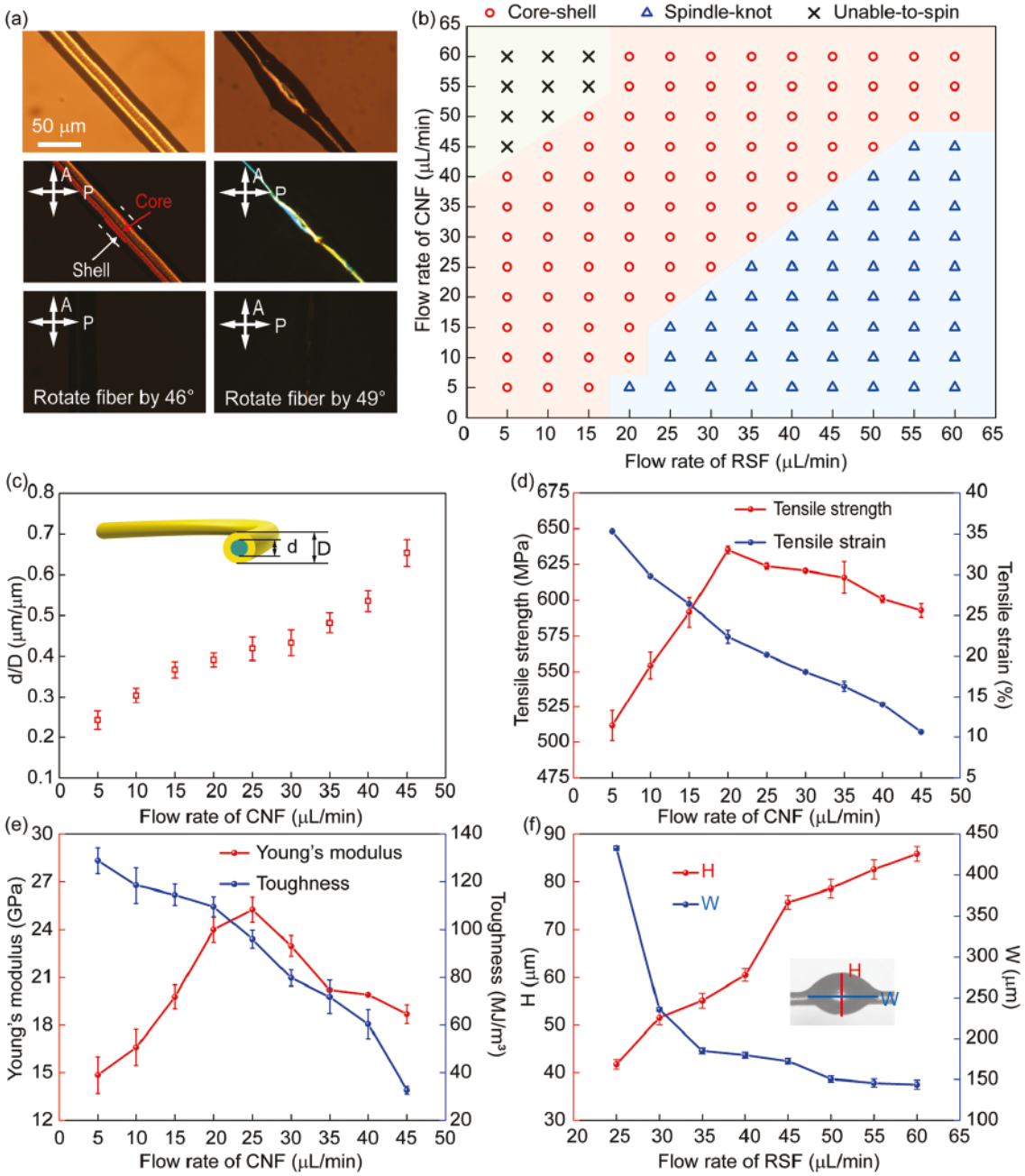

Figure 2. Tunable fiber morphology and mechanical property of hierarchical CNF/RSF fibers via the flow rates of the inner and outer phases. a) POM images of core-shell and spindle-knot fibers prepared using a coaxial microfluidic device. The core-shell structure of CNF/RSF fibers is suggested by the birefringent CNF core and the non-birefringent RSF shell around the core. b) Phase diagram showing different morphologies of hierarchical CNF/RSF fibers prepared under different flow rates. Circles, triangles, and crosses represent core-shell, spindle-knot, and unable-to-spin regimes, respectively. c) Tunable d/D ratio of CNF/RSF core-shell fibers via the flow rate of the inner CNF phase. The flow rate of the outer RSF phase is kept constant at 10 L min^{-1}. d and D are the diameters of the inner core and outer shell, respectively. d,e) Tensile strength, tensile strain, Young's modulus, and toughness of post-stretched core-shell fibers as a function of the flow rate of the inner CNF phase. f) Tunable H and W of spindle-knot fibers via the flow rate of the outer RSF phase. H and W determined from the microscope images represent the spindle's height and width, respectively. The flow rate of the inner CNF phase is kept constant at 15 L min^{-1}.

40 L min^{-1}, wet-spun fibers easily break due to insufficient formic acid from the outer shell to protonate CNFs in the core, resulting in the failure of fiber gelation. The diameters of the inner core and outer shell thus could flexibly be tailored by varying the inner and outer phase flow rates, respectively, as shown in Figure 2c and Figure S10, Supporting Information. Generally, when the outer phase flow rate is kept constant, the diameter of the fiber core increases as the inner phase flow rate increases.

The inner core, which consists of stiff CNFs, mainly contributes to the tensile strength and Young's modulus, while the outer shell, which is composed of elastic RSFs, mainly

contributes to the tensile strain and toughness. Therefore, as the flow rate of the inner CNF phase and thus the fiber's inner core increases, the tensile strength and Young's modulus gradually increase, while the tensile strain and toughness consistently decrease, as shown in Figure 2d and e, Figure S11 and Table S1, Supporting Information. However, when the inner CNF phase flow rate increases beyond an optimal value (20 L min^{-1}), the tensile strain and Young's modulus show a slight decrease, as CNFs in the core are not fully protonated due to limited formic acid from the shell. When optimized, the tensile strength, tensile strain, Young's modulus, and toughness of core-shell fibers are up to 635 MPa, 22.4%, 24.0 GPa, and 110 MJ m^{-3}, respectively; the excellent mechanical performances are attributed to the synergistic effect of the strong CNF core and the tough RSF shell.

For spindle-knot fibers, when the flow rate of the inner CNF phase is kept constant, the spindle's height H increases while the width W decreases, as the flow rate of the outer RSF phase increases, as shown in Figure 2f and Figure S12, Supporting Information. Spindle-knot fibers also demonstrate relatively good mechanical performances and their tensile strength, tensile strain, Young's modulus, and toughness reach 579 MPa, 25.2%, 20.3 GPa, and 106 MJ m^{-3}, respectively, as illustrated in Figure S13, Supporting Information and summarized in Table S2, Supporting Information.

2.3. Enhancing the Mechanical Performances of Core-Shell Fibers by Post-Stretching

CNF/RSF core-shell fibers could be continuously spun and collected on a spool, as shown in Figure 3a. SEM image shows that the core-shell fiber has a uniform diameter and a smooth surface, which could be knotted without any fracture, suggesting a good flexibility, as shown in Figure 3b. Cross section of a core-shell fiber confirms that there is no observable interface between the inner CNF core and the outer RSF shell, demonstrating an excellent integrity, as shown in Figure 3c. CNF/RSF core-shell fibers are tough and strong; a typical core-shell fiber with a diameter of 95 m could easily lift up a 20 g weight, as shown in Figure 3d. Moreover, polarized optical microscopy (POM) images show that the core of core-shell fibers shows a higher birefringence with the increasement of post-stretching ratio, indicating a more orientationally ordered arrangement of CNFs in the core, as shown in Figure S14, Supporting Information.

To further enhance the mechanical performances of as-spun fibers by post-stretching and optimize their performances, stress-strain curves of RSF fibers and CNF/RSF core-shell fibers under different post-stretching ratios are shown in Figure 3e,f, respectively. RSF fibers are prepared using a single-channel microfluidic device (Figures S4b, S15, and S16, Supporting Information), while CNF/RSF core-shell fibers are prepared using a co-axial microfluidic device. RSF fibers and CNF/RSF core-shell fibers show a similar trend in the mechanical property that the tensile strength and Young's modulus increase while the tensile strain decreases, as the post-stretching ratio increases. Generally, post-stretching will induce a more ordered structure along the fiber axis, thus facilitating non-covalent interactions within the fiber matrix and improving the tensile strength and Young's modulus, as summarized in Table 1 and Table S3, Supporting Information. For example, when post-stretched by six times, the tensile strength of core-shell fibers increases from 147 MPa to 635 MPa and the Young's modulus increases from 2.34 GPa to 24.0 GPa. Compared with post-stretched RSF fibers (tensile strength = 390 MPa and Young's modulus = 12.3 GPa) and as-spun CNF fibers (tensile strength = 345 MPa and Young's modulus = 18.9 GPa), as shown in Figures S17, S18, and Table S4, Supporting Information, post-stretched CNF/RSF core-shell fibers demonstrate much better mechanical performances, as shown in Figure 3g and h. Moreover, the tensile strength of post-stretched CNF/RSF core-shell fibers is more than two times higher than natural degummed silks (Figure S19, Supporting Information). The enhancement of mechanical performances by post stretching is attributed to the induced orientational ordering of RSFs in the shell and CNFs in the core, facilitating the formation of more non-covalent interactions within the fibers.

2.4. Characterization of the Ordering within Core-Shell Fibers

SAXS analysis is performed using synchrotron radiation to investigate the underlying mechanism, by which post-stretching treatment can dramatically enhance the mechanical performances of CNF/RSF core-shell fibers. The schematics of the SAXS experimental setup is shown in Figure 4a. 2D SAXS patterns of as-spun and post-stretched CNF/RSF core-shell fibers reveal that the circular scattering halo at small angle becomes more elongated perpendicular to the stretching direction with the increase of post-stretching ratio, suggesting a better alignment and a tighter stacking of fibroins along the stretching direction, as illustrated in Figure 4b. The better alignment and tighter stacking thus facilitate the formation of more non-covalent interactions and enhance the mechanical performances.

To quantitatively characterize the microstructure of post-stretched CNF/RSF core-shell fibers, 1D SAXS profiles of $I(q)$ versus q are extracted along the equator, as shown in Figure 4c. According to Porod's law,[26] the interface factor σ, which characterizes the interface between ordered and disordered domains and is a characteristic parameter to estimate the relative thickness of the mesophase zones, can be extracted from the slope k of $\ln[I(q)q^4]$ versus q^2 plots (Figure 4d), that is, $\sigma = \sqrt{|k|}$.[27] As the post-stretching ratio increases from zero to six times, the interface factor σ increases from 5.23 to 5.73 nm, indicating a larger thickness of the mesophase zones and thus guaranteeing the remarkable mechanical properties, as summarized in Table 2.

When integrated over the azimuthal angle, the SAXS patterns of $B_{obs}{}^2$ versus q^{-2} are shown in Figure 4e. B_φ, the integral breadth of the normal of the scatterer that characterizes the disordering of fibroins, could be analyzed from the plots' intercept b', that is, $B_\varphi = \sqrt{b'}$, and L, the distance between neighboring fibroins, could be calculated from the plots' slope k', that is, $L = 2\pi/\sqrt{k'}$, whose detail derivations are shown in Supplementary Information in Section 3. When the post-stretching ratio increases from zero to six times, the value of B_φ decreases from 38 to 16, suggesting a better ordering in fibril orientation, and the value of L decreases from 3.8 to 2.8 nm, indicating a

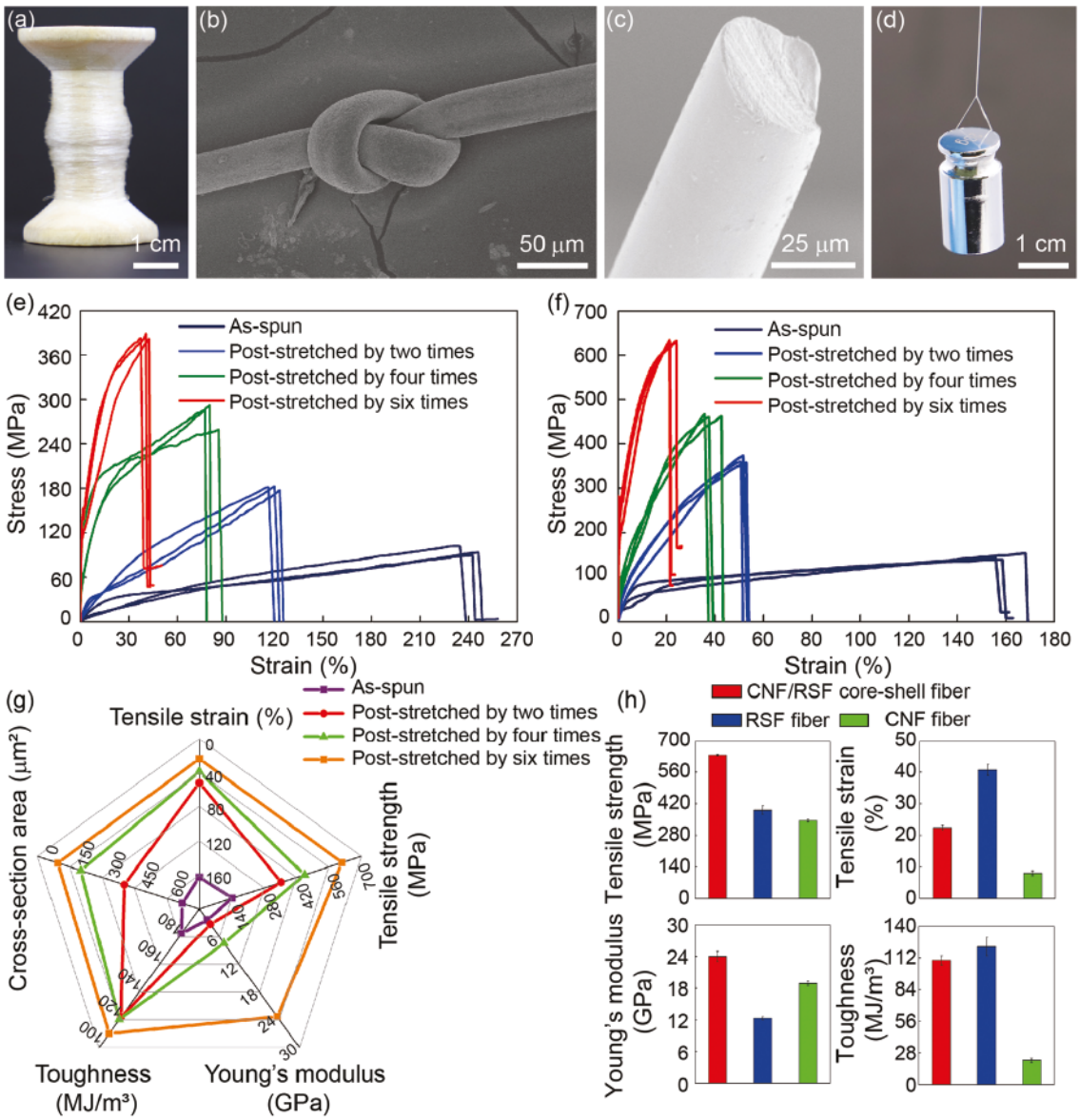

Figure 3. Mechanical performances of as-spun and post-stretched core-shell fibers. a) Photograph of core-shell fibers collected on a spool. b) SEM image of a knotted core-shell fiber. c) SEM image showing the cross section of a core-shell fiber. d) Photograph of a 20 g weight lifted by a core-shell fiber with a diameter of 95 m. e,f) Stress-strain curves of RSF fibers and CNF/RSF core-shell fibers under different post-stretching ratios, respectively. g) Spider chart demonstrating the mechanical performances of core-shell fibers under different post-stretching ratios. Generally, the tensile strength and Young's modulus increase while the tensile strain and toughness decrease, as the post-stretching ratio increases. h) Tensile strength, tensile strain, Young's modulus and toughness of RSF fibers, CNF/RSF core-shell fibers post-stretched by six times, and as-spun CNF fibers. If not specified, core-shell fibers are prepared using an inner phase flow rate of 20 L min^{-1} and an outer phase flow rate of 10 L min^{-1}.

smaller distance between neighboring fibroins. Therefore, post-stretching will induce an increase in σ and a decrease in both B_{φ} and L, contributing to a more ordered structure and facilitating non-covalent interactions between neighboring fibroins for enhanced mechanical performances, as illustrated in Figure 4f and summarized in Table 2.

Table 1. Mechanical properties of core-shell fibers under different post-stretching ratios.

Post-stretching ratio	Tensile strength [MPa]	Tensile strain [%]	Young's modulus [GPa]	Toughness [MJ m^{-3}]	Diameter [m]
As-spun	147 ± 10	163 ± 10	2.34 ± 0.01	182 ± 11	30.2 ± 4.1
By two times	365 ± 10	52.4 ± 0.5	3.24 ± 0.37	122 ± 7	23.4 ± 2.8
By four times	469 ± 13	39.2 ± 4.1	7.27 ± 1.30	120 ± 13	16.5 ± 2.3
By six times	635 ± 3	22.4 ± 0.8	24.0 ± 0.8	110 ± 4	11.3 ± 1.6

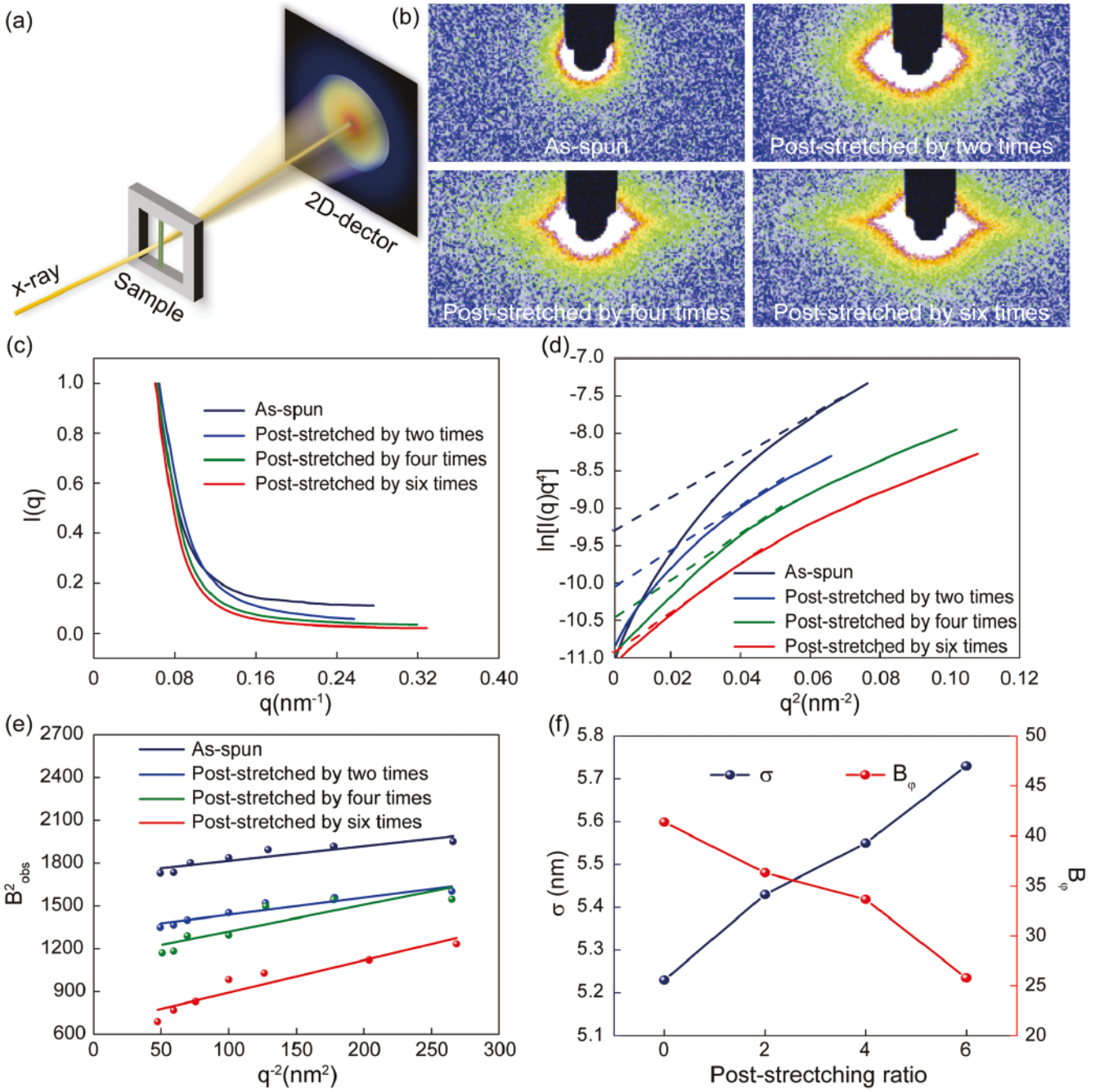

Figure 4. SAXS analysis of core-shell fibers under different post-stretching ratios. a) Schematic representation of the SAXS setup. b) 2D SAXS patterns of as-spun and post-stretched CNF/RSF core-shell fibers. c) 1D profiles of $I(q)$ versus q along the equator of the 2D patterns. q is the scattering vector and $I(q)$ is the scattering intensity. d) Porod-plots of $\ln[I(q)q^4]$ versus q^2. e) Slopes of $B2$ obs versus q^{-2}, where B_{obs} is the integral breadth of the azimuthal profile. f) Dependence of the interface factor, σ, and the integral breadth of the normal of the scatterer, B_{φ}, on the post-stretching ratio.

Table 2. SAXS analysis of core-shell fibers under different post-stretching ratios.

Post-stretching ratio	The interface factor, σ [nm]	The integral breadth, B_{φ}	The distance between neighboring fibroins, L [nm]
As-spun	5.23	38	3.8
By two times	5.43	20	3.6
By four times	5.55	18	3.3
By six times	5.73	16	2.8

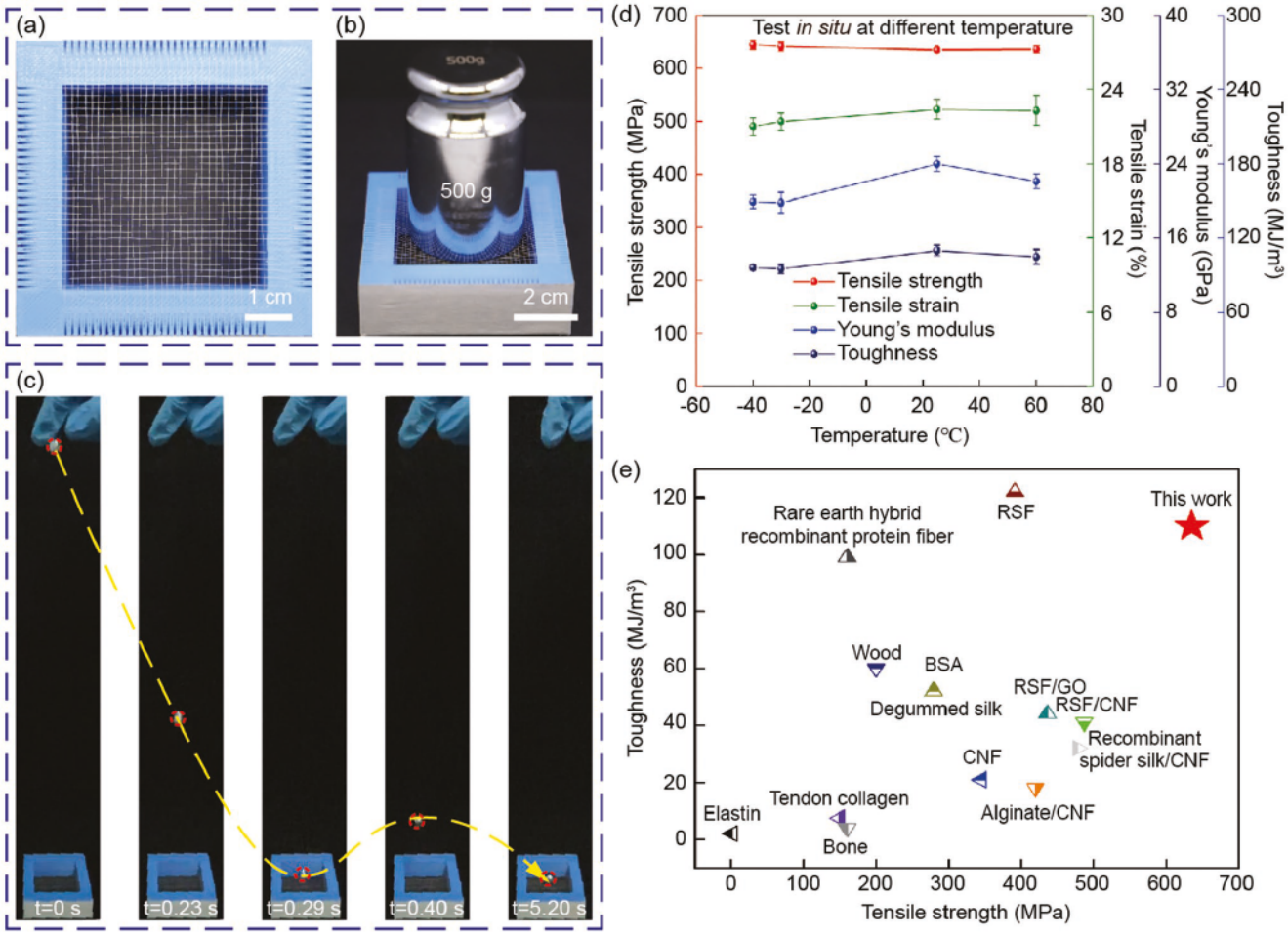

Figure 5. Performances of core–shell fibers against static loading and dynamic impact and under extreme conditions. a) Photograph of a free-standing net woven by as-spun core–shell fibers. b) Static loading of a 500 g weight on the net. c) Dynamic impact of a free-falling steel ball of 7.2 g from a height of 40 cm onto the net. d) Mechanical performances of post-stretched CNF/RSF core–shell fibers tested in situ at different temperatures. e) Comparison of the mechanical performances of core–shell fibers among other reported bio-based fibers.

2.5. Performances of Core–Shell Fibers

CNF/RSF core–shell fibers are tough and strong and could be woven into, for example, a free-standing net, as illustrated in Figure 5a. The fiber net can easily bear a static load of 500 g, which is attributed to the high tensile strength of core–shell fibers, as shown in Figure 5b. In addition to static load, the fiber net can also withstand dynamic impact of a free-falling steel ball of 7.2 g from a height of 40 cm without any damage, suggesting that the fiber net is tough and could absorb the energy of dynamic impact, as shown in Figure 5c. In addition to the superior performances at room temperature, core–shell fibers also show excellent mechanical performances under extreme cold conditions, for example, at –40 and 60 °C. In situ tests of post-stretched core–shell fibers at –40 °C reveal that their mechanical performances barely decrease and their tensile strength, tensile strain, Young's modulus, and toughness remain up to 644 MPa, 21.0%, 19.9 GPa, and 96.1 MJ m^{-3}, respectively, as shown in Figure 5d, Figure S20, Supporting Information and summarized in Table 3. Overall, hierarchical CNF/RSF core–shell fibers demonstrate superior tensile strength and toughness over other regenerated bio-based fibers, and are promising for both fundamental research and practical applications, as shown in Figure 5e and summarized in Table S5, Supporting Information.

Table 3. Mechanical properties of CNF/RSF core–shell fibers post-stretched by six times tested in situ at different temperatures.

Temperature [°C]	Tensile strength [MPa]	Tensile strain [%]	Young's modulus [GPa]	Toughness [MJ m^{-3}]
–40	644 ± 8	21.0 ± 0.7	19.9 ± 0.7	96.1 ± 2.3
–30	641 ± 8	21.4 ± 0.7	19.7 ± 1.1	95.1 ± 3.8
60	636 ± 6	22.3 ± 1.2	22.1 ± 0.8	105 ± 6

3. Conclusion

In summary, by mimicking natural spider silks with a tough core and a stiff shell, hierarchical CNF/RSF core-shell fibers are designed and prepared by wet spinning using a coaxial microfluidic device. Non-covalent interactions, including hydrogen bonding and electrostatic interaction, are introduced between negatively-charged CNFs in the inner core and positively-charged RSFs in the outer shell, diminishing the core/shell interface and forming an integral hierarchical fiber. Meanwhile, shearing in microfluidic channels and post-stretching cause a better ordering of CNFs in the core and RSFs in the shell, thus further enhancing non-covalent interactions within the fiber matrix, as revealed by POM and SAXS studies. By optimizing the parameters, hierarchical CNF/RSF core-shell fibers demonstrate superior strength and toughness over other regenerated bio-based fibers, and can maintain their mechanical properties even at −40 and 60 °C. The method is facile and green, and can continuously prepare strong and tough hierarchical fibers, which are promising for advanced structural materials.

Supporting Information

Supporting Information is available from the Wiley Online Library or from the author.

Acknowledgements

This work was supported by the National Key Research and Development Program of China (YS2021YFC3000089), the Zhejiang Provincial Natural Science Foundation of China (Grant No. Y20B060027), and the National Natural Science Foundation of China (Grant No. 21878258). This work was also supported by the National Science Foundation of United States (DMR-1708729) and the National Science Foundation through the Harvard University MRSEC of United States (DMR-2011754, and DMR-1420570). The authors gratefully acknowledge BL19U2 station of the Shanghai Synchrotron Radiation Facility for the SAXS measurements.

Conflict of Interest

The authors declare no conflict of interest.

Data Availability Statement

The data that support the findings of this study are available from the corresponding author upon reasonable request.

Keywords

biomimetic, core-shell, fiber, hierarchical, microfluidic

Received: September 20, 2022
Published online:

[1] a) C. Feng, C. P. H. Rajapaksha, A. Jokli, *Engineeering* **2021**, *7*, 581; b) C. Guo, C. Li, H. V. Vu, P. Hanna, A. Lechtig, Y. Qiu, X. Mu, S. Ling, A. Nazarian, S. J. Lin, D. L. Kaplan, *Nat. Mater.* **2020**, *19*, 102; c) M. J. Han, D. K. Yoon, *Engineering* **2021**, *7*, 564; d) M. Liu, Y. Zhang, K. Liu, G. Zhang, Y. Mao, L. Chen, Y. Peng, T. H. Tao, *Adv. Mater.* **2021**, *33*, 2004733; e) X. Zhang, Y. Xiao, C. S. Meyer, D. J. O'Brien, S. Ghosh, *Composites, Part B* **2022**, *233*, 109607.
[2] a) X. Y. Du, Q. Li, G. Wu, S. Chen, *Adv. Mater.* **2019**, *31*, 1903733; b) Y. Li, J. Li, J. Sun, H. He, B. Li, C. Ma, K. Liu, H. Zhang, *Angew. Chem., Int. Ed.* **2020**, *59*, 8148; c) J. Sun, J. Chen, K. Liu, H. Zeng, *Engineering* **2021**, *7*, 615.
[3] X. Yang, J. Steck, J. Yang, Y. Wang, Z. Suo, *Engineering* **2021**, *7*, 624.
[4] a) B. Kundu, N. E. Kurland, S. Bano, C. Patra, F. B. Engel, V. K. Yadavalli, S. C. Kundu, *Prog. Polym. Sci.* **2014**, *39*, 251; b) F. G. Omenetto, D. L. Kaplan, *Science* **2010**, *329*, 528; c) L. Pan, F. Wang, Y. Cheng, W. R. Leow, Y. W. Zhang, M. Wang, P. Cai, B. Ji, D. Li, X. Chen, *Nat. Commun.* **2020**, *11*, 1332; d) K. Bourzac, *Nature* **2015**, *519*, S4.
[5] A. Sponner, W. Vater, S. Monajembashi, E. Unger, F. Grosse, K. Weisshart, *PLoS One* **2007**, *2*, e998.
[6] a) K. Augsten, P. Mühlig, C. Herrmann, *Scanning* **2000**, *22*, 12; b) S. F. Li, A. J. McGhie, S. L. Tang, *J. Biophys.* **1994**, *66*, 1209.
[7] a) A. Rising, J. Johansson, *Nat. Chem. Biol.* **2015**, *11*, 309; b) F. Vollrath, *Rev. Mol. Biotechnol.* **2000**, *74*, 67.
[8] a) J. Li, Y. Sun, Y. Liang, J. Ma, B. Li, C. Ma, R. E. Tanzi, H. Zhang, K. Liu, C. Zhang, *CCS Chem.* **2021**, *3*, 1830; b) J. Sun, B. Li, F. Wang, J. Feng, C. Ma, K. Liu, H. Zhang, *CCS Chem.* **2021**, *3*, 1669.
[9] Y. Liu, P. Wu, *Adv. Funct. Mater.* **2020**, *30*, 2002193.
[10] a) F. Barthelat, Z. Yin, M. J. Buehler, *Nat. Rev. Mater.* **2016**, *1*, 16007; b) U. G. K. Wegst, H. Bai, E. Saiz, A. P. Tomsia, R. O. Ritchie, *Nat. Mater.* **2015**, *14*, 23.
[11] C. Cao, Z. Lin, X. Liu, Y. Jia, E. Saiz, S. E. Wolf, H. D. Wagner, L. Jiang, Q. Cheng, *Adv. Funct. Mater.* **2021**, *31*, 2102923.
[12] M. Zhang, M. Zhao, M. Jian, C. Wang, A. Yu, Z. Yin, X. Liang, H. Wang, K. Xia, X. Liang, J. Zhai, Y. Zhang, *Matter* **2019**, *1*, 168.
[13] A. Koeppel, C. Holland, *ACS Biomater. Sci. Eng.* **2017**, *3*, 226.
[14] a) H. Qiu, H. Cheng, J. Meng, G. Wu, S. Chen, *Angew. Chem., Int. Ed.* **2020**, *132*, 8008; b) Y. Yu, S. Bai, S. Wang, A. Hu, *Engineering* **2018**, *4*, 779.
[15] a) Y. Zhang, C. Chen, Y. Qiu, L. Ma, W. Qiu, R. Yu, W. Yu, X. Y. Liu, *Adv. Funct. Mater.* **2021**, *31*, 2100150; b) K. Luo, Y. Yang, Z. Shao, *Adv. Funct. Mater.* **2016**, *26*, 872; c) K. Yazawa, A. D. Malay, N. Ifuku, T. Ishii, H. Masunaga, T. Hikima, K. Numata, *Biomacromolecules* **2018**, *19*, 2227.
[16] a) Z. Chen, H. Zhang, Z. Lin, Y. Lin, J. H. van Esch, X. Y. Liu, *Adv. Funct. Mater.* **2016**, *26*, 8978; b) S. Ling, D. L. Kaplan, M. J. Buehler, *Nat. Rev. Mater.* **2018**, *3*, 18016; c) F. Vollrath, D. P. Knight, *Nature* **2001**, *410*, 541.
[17] N. Mittal, F. Ansari, K. Gowda.V, C. Brouzet, P. Chen, P. T. Larsson, S. V. Roth, F. Lundell, L. Wagberg, N. A. Kotov, *ACS Nano* **2018**, *12*, 6378.
[18] Y. Dou, Z. Wang, W. He, T. Jia, Z. Liu, P. Sun, K. Wen, E. Gao, X. Zhou, X. Hu, J. Li, S. Fang, D. Qian, Z. Liu, *Nat. Commun.* **2019**, *10*, 5293.
[19] a) Y. Liu, J. Ren, S. Ling, *Composites Commun.* **2019**, *13*, 85; b) D. P. Knight, F. Vollrath, *Proc. R. Soc. B* **1999**, *266*, 519.
[20] L. Chen, C. Yang, Y. Xiao, X. Yan, L. Hu, M. Eggersdorfer, D. Chen, D. A. Weitz, F. Ye, *Mater. Today: Proc.* **2021**, *16*, 100136.
[21] a) M. Tsukada, G. Freddi, P. Monti, A. Bertoluzza, N. Kasai, *J. Polym. Sci., Part B: Polym. Phys.* **1995**, *33*, 1995; b) O. N. Tretinnikov, Y. Tamada, *Langmuir* **2001**, *17*, 7406; c) M. Sonoyama, M. Miyazawa, G. Katagiri, H. Ishida, *Appl. Spectrosc.* **1997**, *51*, 545.
[22] N. Mittal, K. G. V. F. Ansari, C. Brouzet, P. Chen, P. T. Larsson, V. R. S, L. F, L. Wagberg, N. A. Kotov, L. D. Söderberg, *ACS Nano* **2018**, *12*, 6378.
[23] D. J. Park, Y. Choi, S. Heo, S. Y. Cho, H. J. Jin, *J. Nanosci. Nanotechnol.* **2012**, *12*, 6139.
[24] X. Duan, J. Yu, Y. Zhu, Z. Zheng, Q. Liao, Y. Xiao, Y. Li, Z. He, Z. Y, H. Wang, L. Qu, *ACS Nano* **2020**, *14*, 14929.
[25] L. Rayleigh, *J. London Math. Soc.* **1878**, *1*, 4.
[26] L. D. Miller, S. Putthanarat, R. K. Eby, W. W. Adams, *Int. J. Biol. Macromol.* **1999**, *24*, 159.
[27] a) C. Zhang, Y. Zhang, H. Shao, X. Hu, *ACS Appl. Mater. Interfaces* **2016**, *8*, 3349; b) H. Pan, Y. Zhang, H. Shao, X. Hu, X. Li, F. Tian, J. Wang, *J. Mater. Chem. B* **2014**, *2*, 1408.

